Pol. J. Environ. Stud. Vol. 30, No. 1 (2021), 257-271
DOI: *10.15244/pjoes/116608* ONLINE PUBLICATION DATE: 2020-09-07

Original Research

Relations between Microtopography and Soil N and P Observed by an Unmanned Aerial Vehicle and Satellite Remote Sensing (GF-2)

Hezhen Lou[1], Xiaoyu Ren[2], Shengtian Yang[1]*, Fanghua Hao[1], Mingyong Cai[3], Yue Wang[4]

[1]College of Water Sciences, Beijing Normal University, Beijing Key Laboratory for Remote Sensing of Environment and Digital Cities, Beijing 100875, China
[2]Beijing Weather Modification Office, Beijing, 100089, China
[3]Satellite Environment Center of MEP, Beijing 100094, China
[4]School of Biological Science, Georgia Institute of Technology, 310 Ferst Dr NW, Atlanta, Georgia, 30332, USA

Received: 22 August 2019
Accepted: 14 January 2020

Abstract

Topography is important for soil nutrient loss and critical source area (CSA) identification. Previous studies have primarily used mass soil sampling to explore the relations between topography and soil nutrients (especially N and P) at the coarse scales. The relations at the microtopographic scale, however, remain unclear. This study integrated unmanned aerial vehicle (UAV) and satellite remote sensing (GF-2) data to create two new indices – NDVI(N) and NDVI(P). Results revealed more pixels with high NDVI(N) values distributed across low elevation difference grades in paddy land; however, this was reversed for dry land. There were more NDVI(P) pixels with large (small) values at high (low) elevation difference grades in the dry land (paddy land). In dry land, the average NDVI(N) was in the range of 0.25-0.33, and NDVI(P) was in the range of 0.47-0.61 for each elevation grade. In paddy land, the average NDVI(N) and NDVI(P) values for each elevation grade were in the range of 0.24-0.32 and 0.31-0.43, respectively. Microtopography can redistribute N and P spatially within the soil because it changes the direction of flow from irrigation and rainfall and of sediment flow from erosion. Furthermore, soil N and P accumulate simultaneously in the soil of agricultural land.

Keywords: GF-2, microtopography, NDVI(N), NDVI(P), soil nutrients, UAV

Introduction

Topography, which reflects the variation in elevation of the earth's surface, has many influences on the allocation of energy and materials [1]. Microtopography which describes the topography on the fine scale also has direct impacts on vegetation and soil [2-3]. For example, microtopography can affect the diversity of vegetation, plant biomass, and chemical elements [4]. The concentration of soil nutrients such as N and P changes with variation of soil moisture, solar energy,

*e-mail: yangshengtian@bnu.edu.cn

and humus content induced by microtopography [5-6]. Meanwhile, topography shapes the land cover, which is one of the most important data used to demonstrate the effects of land use changes, especially human activities [7-8]. Land use maps can be produced via different methods on satellite images [9]. Consequently, microtopography has received considerable attention around the world because of its substantial influence on agricultural management, which is manifested through its critical roles in soil erosion and the loss of soil nutrients (e.g., N and P) [10-11].

Microtopography influences the loss of soil N and P of agricultural land through three principal aspects: runoff confluence, soil erosion, and nutrient loss route [12-13]. Runoff affected by microtopography can change the magnitude of the losses of dissolved N and P, especially in steep areas [5, 14-15]. Runoff changes water stress, which is an important factor in agricultural production [16-18]. Soil erosion is a complex process that can directly and powerfully increase particulate P loss [19-20], and microtopography constitutes a key parameter in soil erosion calculations [21]. Investigation of N and P loss routes is an area of active research because critical source areas (CSAs) can be detected if such routes are known [22-23]. Thus, it is necessary to determine the spatial distributions of N and P at different elevations. Thus, we first need to precisely describe the local microtopography using high spatial-resolution land-elevation data derived from a digital surface model (DSM) and a digital elevation model (DEM) [24]. Knowing the spatial distributions of N and P at different elevations is fundamental to establishing how microtopography might influence their loss processes in agricultural land.

Traditional methods used to explore topographic influence on soil N and P loss processes include soil sampling based on geostatistics, model simulation driven by DEMs, and photogrammetric soil surface measurements [25-27]. Mass soil sampling incorporated with surveying, which is appropriate for field-scale or farm-scale studies, is a method that can derive precise measurements both of soil nutrient concentrations and of land elevations [28-29]. At the watershed and regional scales, ecohydrological models combined with DEMs are often used [30-31], and the DEMs are usually derived from remote sensing data, e.g., the Shuttle Radar Topography Mission [32]. Close-range photogrammetry integrated with plot experiments is also used to explore the relation between soil loss and topography. However, despite obtaining very accurate elevation information, translating the findings derived using this technique to larger scales is difficult because of the small spatial coverage. At the same time, the methods described above cannot meet the requirements of such work because they are too complex or data collection is too difficult. Recently, the development of unmanned aerial vehicles (UAVs) has offered new opportunities for quantifying land elevation precisely. UAVs not only provide cost-efficient solutions but also yield remote sensing data at the sub-decimeter scale spatial resolution and with high spatial accuracy [33-35]. In this study, we aimed to obtain high spatial-

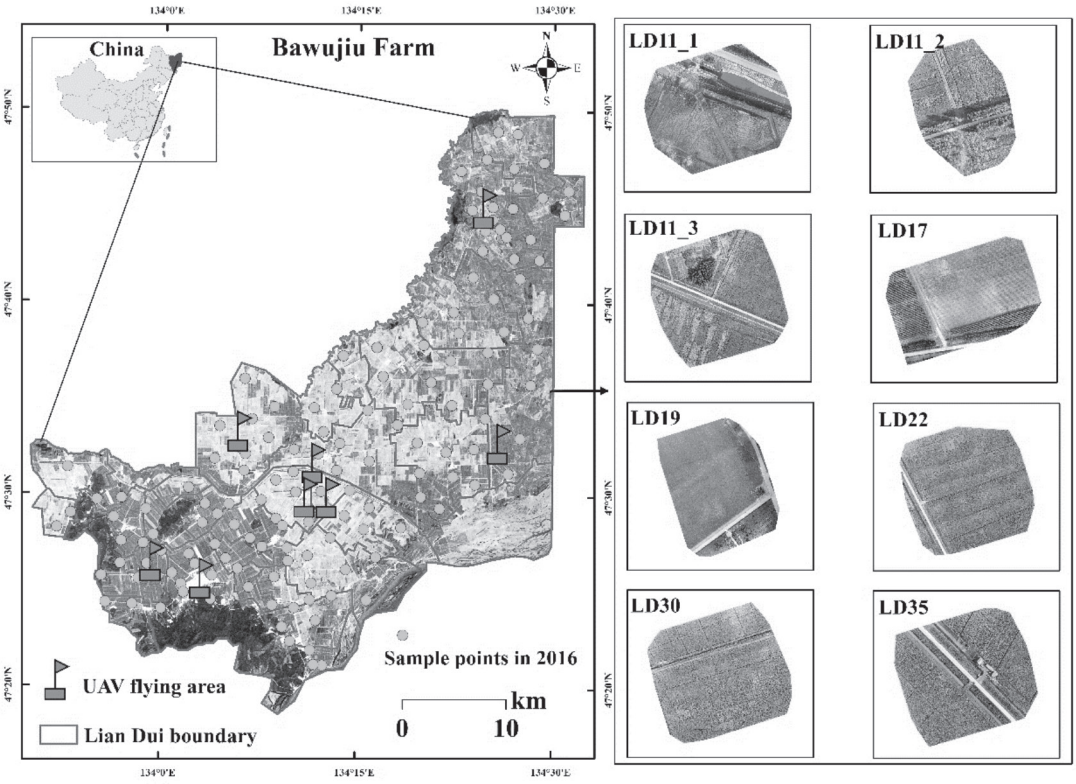

Fig. 1. Study area showing the eight UAV control flying areas and sampling points in 2016 at the Bawujiu Farm.

resolution elevation data precisely and easily to explore how soil N and P are distributed at different elevations and to determine their loss routes.

This research had three primary objectives: 1) to explore the relationship between microtopography and soil N and P, 2) to determine the laws governing the spatial distribution characteristics of soil N and P at microtopographic scale, and 3) to create two new indices to represent the spatial distributions of soil N and P based on GF-2 satellite and UAV data.

Material and Methods

Study Domain

Bawujiu Farm (43°18′-48°50′N, 133°50′-134°33′E), covering an area of 1345 km^2 and located in the northeast of the Sanjiang Plain in China (Fig. 1), served as the experimental area for this study. As one of the national commercial crop bases, Bawujiu Farm has excellent natural conditions for agriculture and a long history of development [23]. Annual precipitation ranges from 500 to 600 mm, and the annual average temperature is 1.9ºC. The climate is humid with a mid-humid continental climate type. Most of Bawujiu Farm is flat and homogenous arable land. There are seven soil types at this farm: calcaric fluvisols, eutric planosols, haplic chernozems, molic gleysols, plinthic lnvisols, glossic chernozems, and chromic luvisols.

As a reflection of its fertile soil and sufficient irrigation conditions, Bawujiu Farm has a long history of intensive agricultural development spanning more than 60 years. The original natural wetlands in this area were transformed to cultivated land and now there are few areas of wetlands left. Agricultural land and forests are the two major land use types on this farm, accounting for 91% and 7% of the total, respectively. Paddy land and dry land are the two leading arable land use types. As a national commercial grain production base, large amounts of fertilizers have been used at the farm over the years because of the large national demand for crops. Therefore, nonpoint source pollution has become a major concern at this farm, e.g., large amounts of P accumulated within the soil would induce leaching of P [11].

At Bawujiu Farm, the Liandui (LD) is the basic management unit. In September 2016, eight UAV control flying areas were implemented in six LDs: LD11_1 (i.e., the 1st control flying area in the 11th LD), LD11_2, LD11_3, LD17, LD19, LD22, LD30, and LD35 (Fig. 1). LD17 and LD19 are dry land areas, and the others are paddy land areas. These two land use types have different irrigation regimes and varying topographic conditions. Dry land at the farm is irrigated by rain, and its surface is not particularly flat, whereas paddy land is irrigated using well irrigation facilities and channels, and its surface is generally flat. Soil sampling was performed in April 2016 to obtain measurements of soil N and P concentrations (Fig. 1).

Framework of this Study

Four main steps were undertaken to explore the relations between microtopography and soil N and P concentrations (Fig. 2). The first step involved retrieving

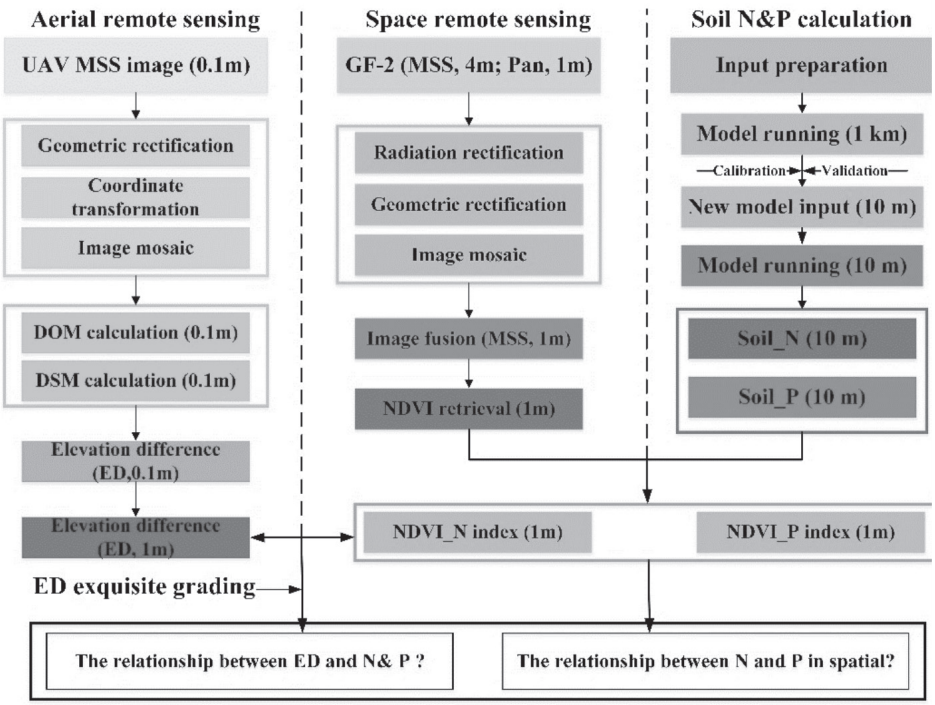

Fig. 2. Flow chart of the study process.

Table 1 Aerial and satellite remote sensing data used in this study.

Space RS	Sensor	Sensor bands	Swath width	Spatial Resolution	Visit cycle	Inclination angle	Image N.
GF-2	Altitude = 631km Solar Synch.	(Pan) 0.45~0.90μm MSS = 4 (B)0.45~0.52μm (G) 0.52~0.59μm (R)0.63~0.69μm (NIR) 0.77~0.89μm	45km (Two cameras combined)	Pan = 1 m MSS = 4 m	5d	±35°	11

RS: remote sensing; MSS: multispectral scanner; R: red; G: green; B: blue; NIR: near-infrared; N.: number; UAV: unmanned aerial vehicle; Pan: panchromatic; GF: Gao Fen satellite; Synch.: synchronous.

microtopographic data using remote sensing imagery obtained by the UAV. Then, these microtopographic data were divided into 10 elevation differences to describe fine-scale topographic variations.

The second step was to obtain soil N and P concentrations using the EcoHAT model. Two main calculation processes at different spatial scales were carried out. One, the model obtains soil N and P concentrations at a 1-km spatial resolution because the in-situ sample grid is of 1 km. Two, for matching the higher spatial resolution of UAV and GF-2 data, soil N and P concentrations from the model at 10 m were also calculated.

The third step was to create a normalized difference vegetation index for N (NDVI(N)) and a normalized difference vegetation index for P (NDVI(P)) to downscale the raster data set of soil N and P concentrations and to explore the relationship between soil N and P concentrations at the microtopographic scale. The NDVI data were retrieved by satellite remote sensing (GF-2).

The fourth step involved exploring the answers to the two questions concerning the relationship between the elevation difference and soil N and P concentrations and the relationship between soil N and P at the microtopographic scale.

Data

Satellite Remote Sensing Data and UAV Data

The satellite remote sensing data (Table 1) used in this study to obtain the NDVI(N) and the NDVI(P) were retrieved by the GF-2 satellite, which is a new-generation high spatial-resolution satellite from China with sensors operating in panchromatic and MSS (i.e. red (R), green (G), blue (B), and NIR) spectral channels. The spatial resolutions of the panchromatic sensor and the MSS are 1 and 4 m, respectively. The platform altitude is 631 km, the swath width is 45 km (two cameras combined), and the visit cycle is 5 days. We used data acquired on May 22, 2016 (inclination angle: ±35°), and 11 images covered the entire study area.

The aerial remote sensing UAV used in this study exhibited better spatial and temporal resolutions than the satellite platform (Fig. 3). The UAV comprises five core components: four airscrews, a control center and global positioning system (GPS), a camera holder, an engine, and an optical camera. The built-in GPS meant that the coordinates of each pixel could be obtained when acquiring images with the camera, which is how the DSM could be derived using the optical remote sensing images. Once the DSM had been obtained, the elevation difference could be easily calculated.

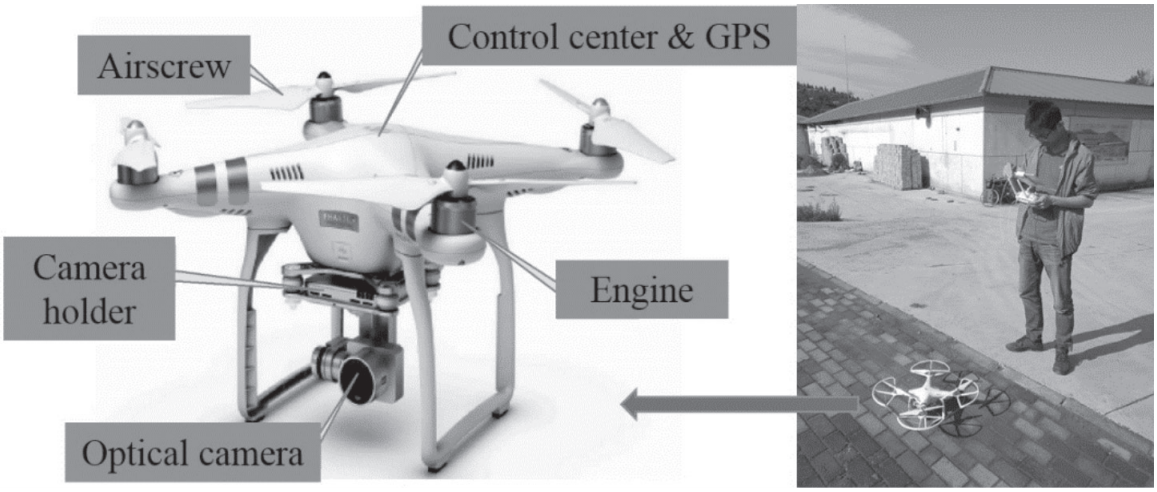

Fig. 3. The UAV and its core components.

Table 2. Details of aerial remote sensing data and the UAV platform used in this study.

Name of flying parameters	Value of flying parameters
UAV type	Phantom-3-pro
Camera type	FC300X
Sensor type	Sony Exmor R CMOS
Camera pixels	40003000
Max aperture	f/2.8
Camera focal length	20 mm
Field of view (FOV)	94°
Max flight height	500m
Flying weight	1280g
Max horizontal speed	16 m/s
Max flying duration time	23 min
Working temperature	0ºC – 40ºC
Sensor bands	3 (R,G,B)
Swath width	171128 m
Altitude	100 m
Resolution	0.042 m
Inclination angle	Orthogonal

Detailed information regarding the core components and imaging capabilities of the UAV used in this research is presented in Table 2. The spatial resolution of the UAV is 0.042 m with a 100-m sensor altitude and a 171 × 128 m swath width. The UAV sensor operates in the R, G, and B spectral channels. The UAV was flown on September 26, 2016, and 360 images were acquired. The inclination angle was orthogonal. According to the performance of the UAV, high spatial-resolution images were obtained, from which the elevation differences in the study area were calculated.

Soil N and P Data

To obtain the spatial concentrations of soil N and P, a single soil sampling campaign was undertaken in late April 2016 at the Bawujiu Farm (see Fig. 1). Overall, 141 soil samples were obtained during the sampling campaign. In the laboratory, prior to air-drying at 25ºC, plant and organic residue and all other visible extraneous material in the soil samples were removed. The dried soil was ground in an agate mortar and then passed through a 2-mm nylon sieve to obtain a sample suitable for chemical analysis. The total soil N concentration was determined using a CHN elemental analyzer (Euro Vector S.P.A EA3000, Milan, Italy) at a burning temperature of 900ºC. The total soil P concentration was determined using the inductively coupled plasma atomic emission spectrometry method (ICP-OES, IRIS Intrepid II XSP, ThermoElectron, USA) after the samples had undergone mixed acid (HF, HNO_3, and $HCLO_4$) digestion [36].

Creation of NDVI(N) and NDVI(P)

NDVI is an advantageous indicator for the concentrations of soil N and P and their variations [37]. NDVI and soil N concentrations have a positive correlation, i.e., a higher NDVI value is associated with a larger amount of N in the soil. In addition, NDVI values are also sensitive to the efficiency of N use by vegetation [38-39]. Similarly, NDVI and soil P concentrations also have a positive correlation, whereby higher NDVI values suggest higher soil P concentrations [40-42].

In this study, two new indices, NDVI(N) (Eq. 1) and NDVI(P) (Eq. 2), were formed to represent the spatial distribution of soil N and P, respectively:

$$NDVI(N_{i,j}) = NDVI_{i,j} \times normalization(N_{i,j}) \quad (1)$$

$$NDVI(P_{i,j}) = NDVI_{i,j} \times normalization(P_{i,j}) \quad (2)$$

...where $NDVI(N_{i,j})$ and $NDVI(P_{i,j})$ are the pixel values of the NDVI(N) and NDVI(P) indices, respectively; $N_{i,j}$ and $P_{i,j}$ are the pixel values of the spatial distribution data of soil N and P, respectively; and i and j are the specified row and column numbers, respectively. These two indices allow downscaling of the coarse data of soil N and P via interpolation.

Based on the measurements collected by the GF-2 sensor, the NDVI could be calculated as follows:

$$NDVI = \frac{\rho NIR - \rho Red}{\rho NIR + \rho Red} \quad (3)$$

...where ρNIR is the fraction of emitted near-infrared (NIR) radiation returned from the vegetation and ρRed is the fraction of emitted red radiation returned from the vegetation [43].

Soil N and P Calculation Using the EcoHAT Model

The EcoHAT model [11, 20, 23, 44] includes two major processes, the soil N and P-cycle and the plant N and P-cycle. The soil N cycle includes nitrogen in the rainfall model, nitrogen fertilization model, nitrogen mineralization and decomposition model, nitrogen nitrification and ammonia volatilization model, and nitrogen denitrification model. A fertilization model, a mineralization and a decomposition model, and an inorganic P absorption model are integrated to describe the soil P-cycle process. The net primary productivity (NPP) simulation model, a vegetation production distribution model, a vegetation N and P absorption model, and a vegetation litter model are coupled to

Table 3. Functions and parameters in the N and P model.

No.	Model Name	Equation	References
1	N in Rainfall	$N^{rain} = 0.01 \cdot R^{NO3} \cdot R^{day}$	SWAT model [45]
2	N Fertilization	$NO3_{fert} = fert_{minN} \cdot (1 - fert_{NH4}) \cdot fert$ $NH4_{fert} = fert_{minN} \cdot fert_{NH4} \cdot fert$ $orgN_{frsh,fert} = 0.5 \cdot fert_{orgN} \cdot fert$ $orgN_{hum,fert} = 0.5 \cdot fert_{orgN} \cdot fert$	SWAT model [45]
3	N Mine & Dec.	$N_{minf,ly} = 0.8 \cdot \delta_{ntr,ly} \cdot orgN_{fresh,ly}$ $N_{dec,ly} = 0.2 \cdot \delta_{ntr,ly} \cdot orgN_{fresh,ly}$	SWAT model [45]
4	N Nit.&Am.Vol.	$N_{nit,ly} = \frac{fr_{nit,ly}}{(fr_{nit,ly} + fr_{vol,ly})} \cdot N_{nit\|vol,ly}$ $N_{vol,ly} = \frac{fr_{vol,ly}}{(fr_{nit,ly} + fr_{vol,ly})} \cdot N_{nit\|vol,ly}$	SWAT model [45]
5	N Denitrification	$D_a = D_p \cdot f_N \cdot f_s \cdot f_T \cdot f_{pH}$	Denitrification Model [46]
6	P Fertilization	$P_{solution,fert} = fert_{minP} \cdot fert$ $orgP_{frsh,fert} = 0.5 \cdot fert_{orgP} \cdot fert$ $orgP_{hum,fert} = 0.5 \cdot fert_{orgP} \cdot fert$	SWAT model [45]
7	P Mine & Dec.	$P_{mina} = 1.4 \cdot \beta_{min} \cdot (\gamma_{tmp}, \gamma_{sw})^{1/2} \cdot orgP_{act}$	[47]
8	Inorganic P absorption	$P_{sol/sta,ly} = \begin{cases} P_{solution,ly} - minP_{act,ly} \cdot \frac{pai}{1-pai} \\ 0.1 \cdot \left(P_{solution,ly} - minP_{act,ly} \cdot \frac{pai}{1-pai}\right) \end{cases}$	SWAT model [45]
9	NPP Simulation	$NPP(x,t) = APAR(x,t) \times \varepsilon(x,t)$	CASA model [48]
10	Vegetation Production distribution	$\frac{dF_B}{dt} = R_{LA\_W} \frac{\varepsilon_{LA}}{dt}$ $\frac{dR_B}{dt} = K_{ra}\left(\frac{dNPP}{dt} - \frac{dF_B}{dt}\right)$ $\frac{dW_B}{dt} = \frac{dNPP}{dt} - \frac{dF_B}{dt} - \frac{dR_B}{dt}$	ForNBM model [49]
11	Nutrient absorption	$X_{uptale} = min(X_{avail}, X_{dem})$	ForNBM model [49]
12	Vegetation Litter	$L_{lit} = \begin{cases} a_{fh}F_b, & T_{air} > T_{fall} \\ F_b, & T_{air} < T_{fall} \\ a_{fs}F_b, & T_{air} > T_{fall} \end{cases}$	$L_{lit} = \begin{cases} a_{fl}FL, & T_{air} > T_{fall} \\ FL, & T_{air} < T_{fall} \end{cases}$ $W_{lit} = a_{fw}W_B$ $R_{lit} = a_{fr}R_B$	ForNBM model [49]

Annotation: N_{rain}: Nitrate added by rainfall(kg N·ha); $\mathbf{R_{NO3}}$: The concentration of nitrogen in the rain(mg N·L); $\mathbf{R_{day}}$: The amount of precipitation on a given day(mm); $\mathbf{NO3_{fert}}$**:** The nitrate added in the soil comes from fertilization(kg N·ha); $\mathbf{fert_{min\ N}}$**:** The percentage of mineral N in fertilization(%);$\mathbf{fert_{NH4}}$**:** The percentage of mineral ammonia nitrogen in fertilization(%);$\mathbf{NH4_{fert}}$**:** The ammonia nitrogen added in the soil comes from fertilization(kg N·ha); **fert:** The amount of fertilization(kg N·ha); $\mathbf{orgN_{frsh,\ fert}}$**:** The fresh organic N in soil comes from fertilization(kg N·ha); $\mathbf{fert_{org\ N}}$**:** The percentage of organic N in fertilization(%);$\mathbf{orgN_{hum,\ fert}}$**:** The humus organic soil N comes from fertilization(kg N·ha); $\mathbf{N_{minf,ly}}$**:** The nitrogen mineralized from the fresh organic N pool(kg N·ha); **:** The residue decay rate constant; $\mathbf{N_{dec,ly}}$**:** The nitrogen decomposed from the fresh organic N pool(kg N·ha); $\mathbf{N_{nit,ly}}$**:** The amount of nitrogen converted from NH_4 to NO_3 in layer ly(kg N·ha); $\mathbf{N_{vol,ly}}$**:** The amount of nitrogen converted from NO_3 to NH_4 in layer ly(kg N·ha); $\mathbf{fr_{nit,ly}}$**:** The estimate fraction of nitrogen lost by nitrification; $\mathbf{fr_{vol,ly}}$**:** The estimate fraction of nitrogen lost by volatilization; **:** The amount of ammonium convert via nitrification and volatilization in layer ly(kg N·ha); $\mathbf{D_a}$**:** The actual denitrification rate(kg $N \cdot m^{-2} \cdot d^{-1}$); $\mathbf{D_p}$**:** The potential denitrification rate(kg $N \cdot m^{-2} \cdot d^{-1}$); $\mathbf{f_N}$**:** The nitrate attenuation function in soil[0-1]; $\mathbf{f_S}$**:** The water attenuation function in soil; $\mathbf{f_T}$**:** The temperature attenuation function in soil; $\mathbf{f_{pH}}$**:** The acid-base property attenuation function in soil; **APAR(x, t):** Plant absorbed photosynthetically active radiation from pixel x in day t($MJ \cdot m^{-2}$); **e(x, t):** The real efficiency of radiation utilization($gC \cdot MJ^{-1}$); **NPP:** Net Primary Productivity($gC \cdot m^{-2}$); $\mathbf{F_B}$**:** NPP the leaf obtain(g $C \cdot m^{-2}$); $\mathbf{R_{LA\_W}}$**:** Biomass in 1 m^2 leaf($g \cdot m^{-2}$);**:** Leaf area increment per month(m^{-2}); $\mathbf{R_B}$**: T**he NPP root obtain($gC \cdot m^{-2}$); $\mathbf{K_{ra}}$**:** Return coefficient of leaf nutrient, constant; $\mathbf{W_B}$**: T**he NPP limb obtain(g $C \cdot m^{-2}$); $\mathbf{X_{avail}}$**:** The plant available amount of element X(X = P)($g \cdot m^{-2}$); $\mathbf{X_{dem}}$**:** The plant demand amount of element X(X=P)($g \cdot m^{-2}$); $\mathbf{L_{lit}}$**:** Leaf wither amount(g $C \cdot m^{-2}$); $\mathbf{a_{fh}}$**:** Deciduous species wither threshold; $\mathbf{a_{fs}}$**:** Evergreen species wither threshold; $\mathbf{a_{fr}}$**:** Root wither threshold**; afw:** Limb wither threshold**; afl:** Herbage wither threshold**;** $\mathbf{T_{air}}$**:** Air temperature(ºC); $\mathbf{T_{fall}}$**:** The threshold temperature of Deciduous species(ºC); $\mathbf{R_{lit}}$**:** The root wither amount(g $C \cdot m^{-2}$); $\mathbf{W_{lit}}$**:** The limb wither amount($gC \cdot m^{-2}$); $\mathbf{L_{lit}}$**:** Herbage wither amount(g $C \cdot m^{-2}$); $\mathbf{F_L}$**: T**he NPP herbage obtain(g $C \cdot m^{-2}$); $\mathbf{T_{fall}}$**:** The threshold temperature of herbage species(ºC); $\mathbf{P_{slution,\ fert}}$**:** The dissolved soil P comes from fertilization(kg P·ha); $\mathbf{fert_{min\ P}}$**:** The percentage of mineral P in fertilization(%); $\mathbf{orgP_{frsh,\ fert}}$**:** The fresh organic P in soil comes from fertilization(kg P·ha); $\mathbf{fert_{org\ P}}$**:** The percentage of organic P in fertilization(%);

Table 3. Continued.

$orgP_{hum, fert}$: The humus organic soil P comes from fertilization(kg P·ha); **P_{mina}:** The phosphorus mineralized from the humus active organic P pool(kg P·ha); **$orgP_{act}$:** The amount of phosphorus in the active organic pool((kg P·ha)); **:** The rate coefficient for mineralization of the humus active organic nutrients; **:** The nutrient cycling temperature factor; **:** The nutrient cycling water factor; **$P_{sol/act, ly}$:** Amount of phosphorus transferred between the active and stable mineral pools(kg P·ha); **$P_{slution, ly}$:** The amount of phosphorus in solution(kg P·ha); **$minP_{act, ly}$:** The amount of phosphorus in the active mineral pool(kg P·ha); **pai:** The phosphorus availability index.

describe the vegetation N- and P-cycle processes. All the arithmetical equations are enumerated in Table 3.

The main input data include multisource remote sensing data and production, meteorological data, and statistical data [23]. In this study, two calculation processes with different spatial scales were carried out. First, the model obtains the soil N and P concentrations at a 1 km spatial resolution because the *in-situ* sample grid is of 1 km. Second, for matching the higher spatial resolution of UAV and GF-2 data, soil N and P concentrations from the model at 10 m were also calculated.

The creation of the NDVI(N) and the NDVI(P) allowed data downscaling. An NDVI at 1-m resolution can describe vegetation and soil nutrient information in detail and provide spatial heterogeneity. To obtain an NDVI with 1-m resolution from the GF-2 data, an image mosaic was created. Then, image fusion was applied to the multispectral scanner (MSS; 4-m resolution) and panchromatic (1-m resolution) data retrieved by the GF-2 satellite (Fig. 2). Output of the EcoHAT model was a raster data set with a 10-m spatial resolution. This resolution was selected based on the mass soil sample numbers and the homogeneity of the land surface. For matching the resolution of the NDVI, the interpolation data were resampled at a 1-m resolution. Based on the relations between NDVI and soil N and P, NDVI(N) and the NDVI(P) were obtained via spatial multiplication in ArcGIS10.2 (Fig. 2). Soil N and P were also downscaled from 10- to 1-m resolution to match the NDVI data. After spatial multiplication between the NDVI and the nutrient data, the two new indices containing information on vegetation and soil nutrients were produced at refined spatial resolution (i.e., 1 m).

Fine-Scale Elevation Grading

The elevation difference as microtopographic information was calculated from the UAV images that also contained elevation information (Fig. 3). First, the overlapped UAV images were processed using PIX4D software (https://pix4d.com/). Then, a digital orthophoto model, DSM, and a point cloud image were obtained. Second, the DEM was calculated from the DSM using the minimum value filtering algorithm (Eq. 4). The height raster of the surface features was produced by subtracting the DEM from the DSM, as follows:

$$DEM_{i,j} = Min\{I_{i,j} | i,j = \frac{N-1}{2}, 1, 2, \cdots, M - \frac{N-1}{2}\} \quad (4)$$

...where $DME_{i,j}$ is the pixel value after filtering; i and j are the specified row and column numbers, respectively; $I_{i,j}$ is the value of the pixel; M is the maximum row or column number; and N is a positive odd number in the form N × N, which refers to the size of the filtering window. Third, the elevation difference was calculated by subtracting the minimum elevation from the DEM in each control flying area (Eq. 5):

$$ED_{i,j} = DEM_{i,j} - ME_{i,j} \quad (5)$$

...where $ED_{i,j}$ refers to the elevation difference in each pixel and $ME_{i,j}$ refers to the pixel that has the minimum elevation.

To explore the impact of microtopography on soil N and P concentrations and to take full advantage of the high-resolution data from the UAV, the elevation differences were graded into 10 groups with 0.02-m increments, and the matched NDVI(N) and NDVI(P) were extracted at the same time. The 10 groups of elevation difference included 0.02–0.04, 0.04–0.06, 0.06–0.08, 0.080–0.10, 0.10–0.12, 0.120–0.14, 0.14–0.16, 0.16–0.18, 0.18–0.20, and LT0.20 m (larger than 0.20).

Data Analysis

Spatial correlation analysis was applied in this study to explore the relationships between elevation difference and both NDVI(N) and NDVI(P). The formulas used for the calculation of covariance and correlation were as follows:

$$Cov_{i,j} = \frac{\sum_{k=1}^{N} (Z_{i,k} - \mu_i)(Z_{j,k} - \mu_j)}{N - 1} \quad (6)$$

$$Corr_{i,j} = \frac{Cov_{i,j}}{\delta_i \delta_j} \quad (7)$$

...where $Cov_{i,j}$ and $Corr_{i,j}$ are the covariance and correlation of a set of bands; Z is the value of a cell; i and j are the layers of a stack; μ is the mean of each layer; N is the number of the cell; k denotes a particular cell; and δ is the standard deviation of a layer.

Results and Discussion

Validation of UAV Data and Model Performance

Data used to validate the DEM derived from the UAV were collected from 22 ground control points

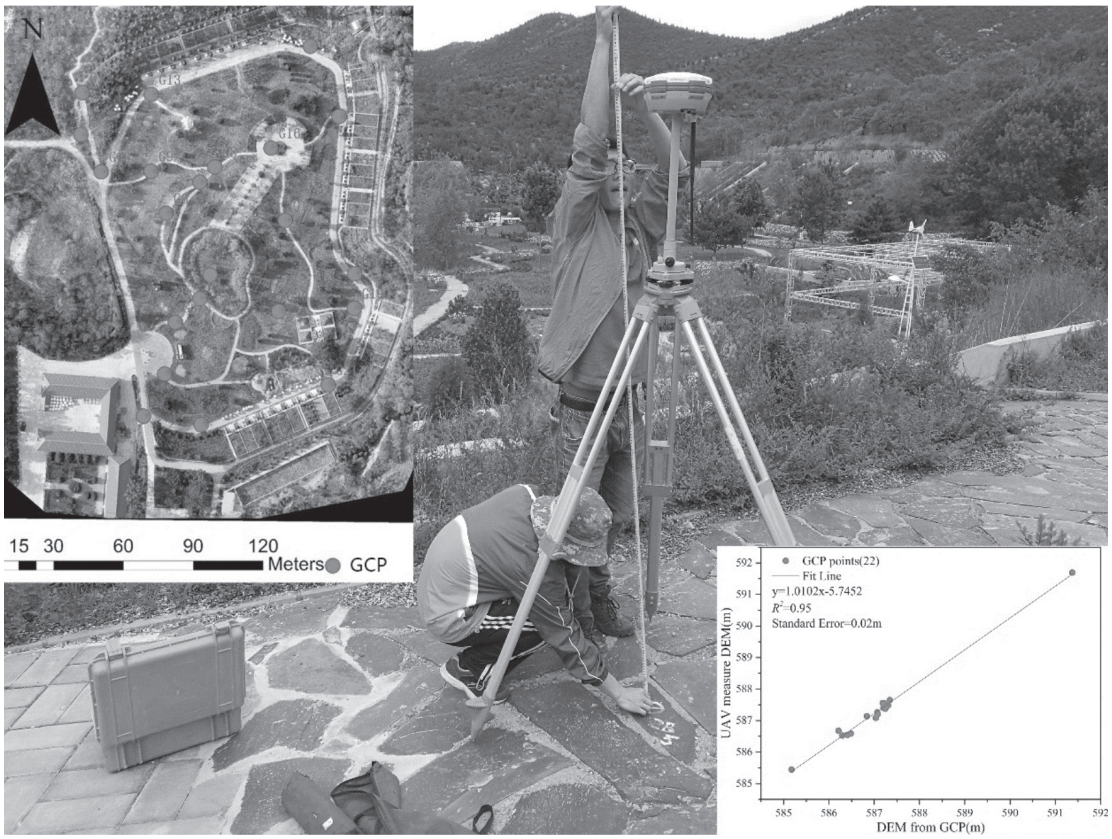

Fig. 4. Ground control points (GCPs) and validation of the DEM derived from UAV data.

(GCPs) (Fig. 4) distributed uniformly at the experiment station (28,000 m²) and Bawujiu Farm (Fig. 4). To obtain the real elevations of the GCPs, real-time kinetic (RTK, ZHD-V30-GNSS-RTK) survey technology was employed (Fig. 4). The GCP values were compared with the DEM values retrieved from the UAV images. The DEM values comprised digital numbers of the pixels in which the GCPs were located, which were extracted using the spatial analysis tool in ArcGIS 10.2. The results showed the DEM derived from the UAV images was valid and could be used in this research (Fig. 4). The average value of the RTK survey data was 587.14 m, and the average value of the UAV data was 587.36 m; the standard deviations of the RTK survey data and the UAV data were 1.05 and 1.07 m, respectively. The R^2 value between the surveyed elevation and the DEM value from the UAV data was 0.95, and the standard error was 0.02 m.

We also validated the simulation results of the model at a 1-km spatial resolution (Fig. 5) by using the sample data in the Bawujiu Farm. The sampling points were spatially unfolded according to their geographic coordinates and then overlaid on the simulation results. The pixel values where the sample points were

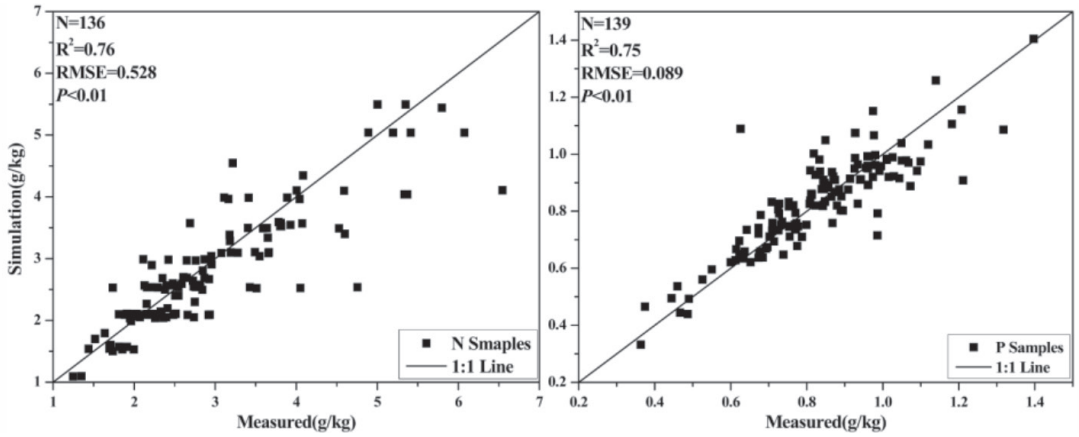

Fig. 5. The validation results of EcoHAT-N and EcoHAT-P.

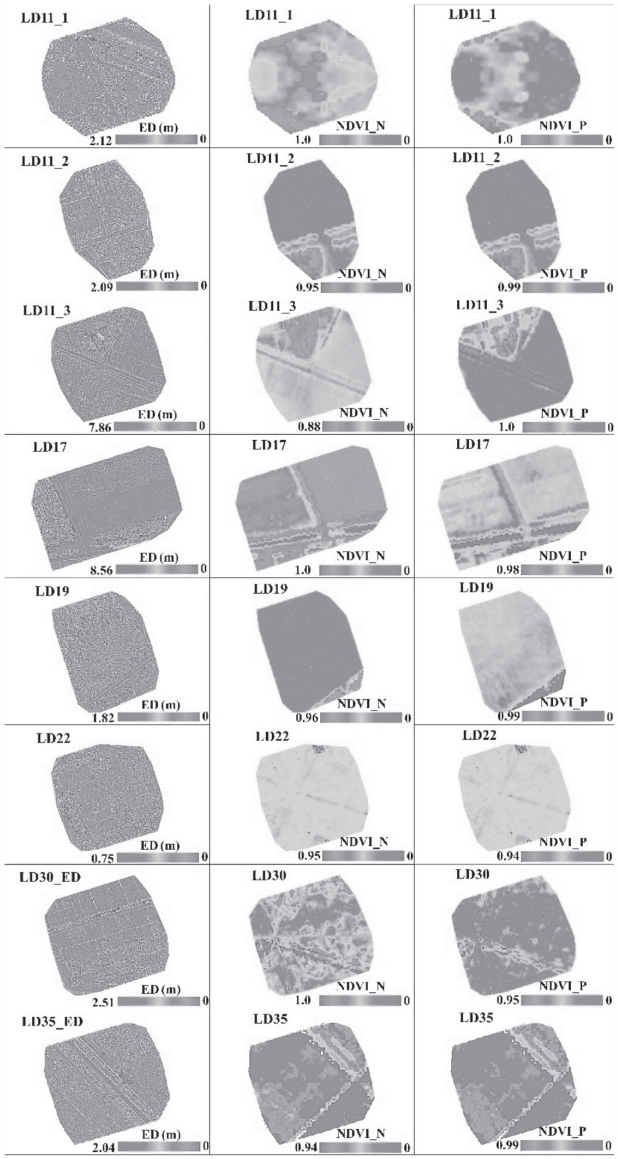

Fig. 6. Spatial distribution of elevation difference, NDVI(N), and NDVI(P) in the eight UAV control flying areas.

located were extracted by the spatial analysis tool in ArcGIS10.5.

The determination coefficients were used to evaluate the simulation results from EcoHAT (Fig. 5, N left; P right). The value of the determination coefficient between the simulated N concentration in the soil from EocHAT and the measured N concentration was 0.76. For P, the value of the determination coefficients between the simulated P concentration in the soil from EocHAT and the measured P concentration was 0.75. The value of R^2 from N was better than that from P because there were more reactive values from the P simulation results in this area. But the root mean square error (RMSE) of the validation of P was 0.089 and that of the validation of N was 0.528. It is better to analyze P than nitrogen because there are more values that drift away from the 1:1 line in the validation of N than those in the validation of P. In other words, the upper validation of the model's simulation results show that the model is stable and meets the requirements of this study.

Spatial Distribution of Elevation Difference and the Two Indices

The spatial distribution of the elevation difference, NDVI(N), and NDVI(P) in the eight UAV control flying areas are presented in Fig. 6. NDVI(N) and the NDVI(P) display similarity in their spatial distribution, whereas the elevation differences in the eight areas are different. In arable land, irrespective of whether land was dry or paddy, the elevation differences were very small, except when related to artificial cement roads, banks of irrigation ditches, and big ridges in the land. In LD11_3 and LD17, the maximum elevation difference reached 7.86 and 8.56 m, respectively. This is because there are tall coniferous forests growing on hills in these two LDs. In the other six LDs, the elevation differences are no greater than 2.51 m.

The spatial distributions of the two indices show similar characters, although their ranges differ in the forested land. Furthermore, LD11_2, LD22, and LD 35 were more similar spatially. The values of both indices are larger in LD17 than in LD11_3. Moreover, the NDVI(N) and NDVI(P) values are substantially higher in ditches than in flat arable land, although in artificial ditches constructed with cement, the values are lower (LD11_1, LD11_3, and LD17). Compared with the high spatial similarity between these two indices, the spatial texture between the two indices and the ED represent more differences. The ED images display more detailed land surface information than the images of the indices. At the same time, the digital number range of the ED is larger than the two indices.

Spatial correlations of NDVI(N) and NDVI(P), elevation difference and NDVI(N), and elevation difference and NDVI(P) were calculated using Eq. (7) (Table 4). A high correlation was observed between NDVI(N) and NDVI(P), consistent with their similar spatial distributions (Fig. 6). The maximum value of 0.89 was obtained in LD11-2, and the minimum value of 0.69 was obtained in LD11_3. Dry land and paddy land show differences in the relationship with NDVI(N) and NDVI(P), i.e., paddy land presents a higher correlation with the indices than dry land. In comparison with the correlation between these two indices themselves, their correlations with elevation differences are lower, i.e., most are negative except for LD17 and LD19. Therefore, elevation difference has a negative correlation with the spatial distribution of NDVI(N) and NDVI(P) in paddy lands, indicating that soil N and P concentrations have negative relationships with microtopography in this land type. However, in dry land, the spatial correlations were positive, which denotes that soil N and P concentrations have negative relationships with microtopography.

Table 4. Spatial correlations of NDVI(N) and NDVI(P), elevation difference and NDVI(N), and elevation difference and NDVI(P).

NDVI(N/P)	S-C	NDVI(N)/ED	S-C	NDVI(P)/ED	Correlation
N._N_11_1	0.71	N._N_11_1	-0.19	N._P_11_1	-0.21
N._N_11_2	0.89	N._N_11_2	-0.35	N._P_11_2	-0.33
N._N_11_3	0.69	N._N_11_3	-0.18	N._P_11_3	-0.19
N._N_17	0.70	N._N_17	0.23	N._P_17	0.29
N._N_19	0.76	N._N_19	0.30	N._P_19	0.44
N._N_22	0.81	N._N_22	-0.36	N._P_22	-0.38
N._N_30	0.66	N._N_30	-0.15	N._P_30	-0.14
N._N_35	0.79	N._N_35	-0.22	N._P_35	-0.29

Annotation: S-C: Spatial Correlation; N.: NDVI; ED: elevation difference.

Statistical Analysis of Soil N and P Concentrations at Microtopography Scale

Numerical regression analyses between NDVI(N) and NDVI(P) were applied using all the pixels in the eight UAV control flying areas (Fig. 7). There were 118,529 pixels in total that could reasonably accurately describe the relationship between NDVI(N) and NDVI(P) at the microgeographic scale. The coefficient of determination (R^2) and RMSE were 0.75 and 0.08, respectively, suggesting a good correlation. However, NDVI(P) has a more standard Gaussian distribution than NDVI(N). The range of NDVI(N) and NDVI(P) values were from 0 to 1. Most NDVI(N) values were located within the range 0–0.6, while most NDVI(P) values were located within the range 0–0.83, and a stronger correlation could be observed within these ranges.

We observed a positive correlation between soil N and P concentrations in agriculture land at the microtopographic scale (Fig. 7). Analysis of the two indices, NDVI(N) and NDVI(P) and the use of UAV data as a "magnifying glass" produced a clear conclusion regarding the relationship between soil N and P concentrations at the fine scale. We calculated the correlation between soil N and P and found the coefficient of correlation value was very low; however, the coefficient of determination between NDVI(N) and NDVI(P) was 0.76. A number of explanations could account for this finding. First, the NDVI could directly reflect soil N [50-51] and P concentrations [52-53] and the nutrient absorption efficiency of vegetation [38]. Based on this, the NDVI(N) and the NDVI(P) could also indicate the concentration and variation of soil N and P concentrations, respectively. Second, analysis at the microtopographic scale provided an opportunity to describe soil nutrient information. The UAV provided high spatial-resolution topographic data [33], which allowed us to derive information about the status and variation of soil nutrients more precisely and thus to generate statistical results with improved accuracy. Meanwhile, the overall range was small because of the short cruising time of the UAV and the high resolution. In the small study area, the variation of topography and soil nutrients was not significant. From Tobler's first law of geography, spatially closer values are related more strongly than more distant ones [54]. Third, intensive agricultural activities also contribute to this relationship. Intensive agricultural activities lead to artificial accumulation of N and P in the soil, especially P, which is generally limited under natural conditions [21].

Relationships between Elevation Difference and Soil N and P

Quantitative statistical distributions of NDVI(N) values at 10 elevation difference grades in the eight

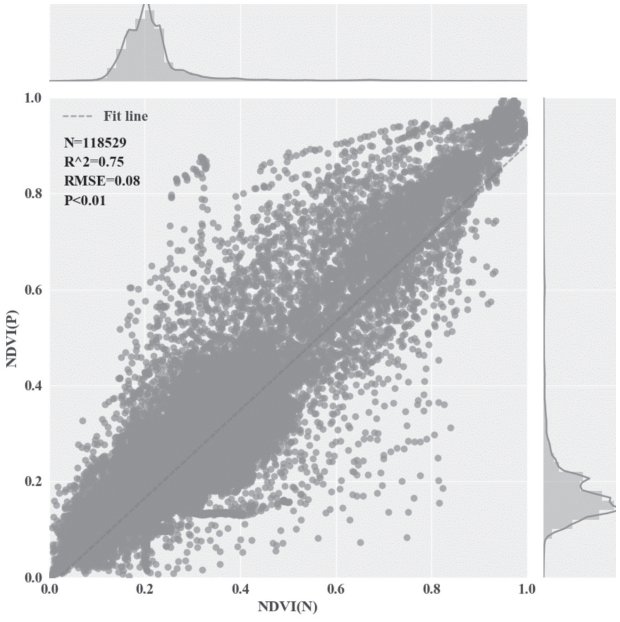

Fig. 7. Numerical regression analysis of the eight UAV control flying areas.

Table 5. Statistics of pixel number in each elevation grade and average values of NDVI(N) and NDVI(P) in each grade in the two cultivated land types.

ED grade (m)	Pixel N. D.land	D.land NDVI(N)	D.land NDVI(P)	Pixel N. P.land	P.land NDVI(N)	P.land NDVI(P)
ED1 (0.02-0.04)	19,273	0.44	0.48	37,663	0.25	0.36
ED2 (0.04-0.06)	8,440	0.45	0.50	15,429	0.26	0.37
ED3 (0.06-0.08)	5,006	0.46	0.53	7,777	0.26	0.37
ED4 (0.08-0.10)	3,077	0.47	0.56	3,644	0.25	0.37
ED5 (0.10-0.12)	1,982	0.47	0.54	1,932	0.22	0.32
ED6 (0.12-0.14)	1,288	0.49	0.57	1,011	0.28	0.38
ED7 (0.14-0.16)	963	0.49	0.59	701	0.27	0.39
ED8 (0.16-0.18)	744	0.49	0.59	405	0.26	0.38
ED9 (0.18-0.20)	556	0.48	0.57	262	0.24	0.34
ED10 (LT 0.20)	6,524	0.50	0.61	1,852	0.26	0.38

N.: number; D.land: dry land; P.land: paddy land.

UAV control flying areas are presented in Fig. 8 and Table 5. In paddy land, there are more pixels with high NDVI(N) values distributed at low elevation difference grades (i.e., ED1, ED2, ED3, and ED4), whereas in dry land, there are more pixels with low NDVI(N) values distributed at low elevation difference grades. This indicates that the soil of cultivated land with low elevation difference has more N in paddy land, whereas the converse is true in dry land. The eight areas were classified as dry land or paddy land because these are the two major agricultural land use types. However, they also have different irrigation regimes and varying topographic conditions. Dry land is irrigated by rain, and its surface is not particularly flat, whereas paddy land is irrigated using well irrigation facilities and channels, and its surface is generally flat.

Although more pixels with higher NDVI(N) values are distributed at low elevation difference grades, irrespective of whether the land is dry or paddy, the distribution of NDVI(N) in the two land use types is different. In dry land, the variation of the distribution of NDVI(N) values is uniform across different elevation grades; the average NDVI(N) value of each grade is 0.45-0.53. In paddy land, more pixels with high NDVI(N) values are distributed in low elevation difference grades, which indicates that the soil N content increases as the elevation of the cultivated land decreases. The average NDVI(N) values are in the range 0.44–0.52 mg/kg. The elevation difference grade of 0.08–0.10 m is the threshold, i.e., there is more N in the paddy land soil at elevation difference grades lower than this threshold.

The NDVI(P) values at 10 ED grades in the eight UAV control flying areas are presented (Fig. 9). There are more pixels with high values at high ED grades in dry land and more pixels with small values at low ED grades in paddy land (Table 4). Although the distribution of NDVI(P) values is obviously different for the two cultivated land use types, the variation law of the distribution of NDVI(P) values in each land use type is clear and significant. In dry land, there is more P content when the ED increases; the average

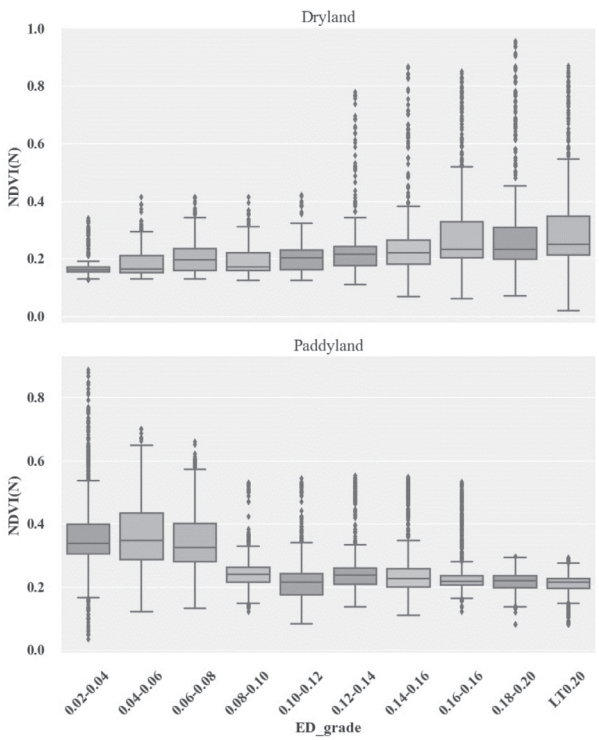

Fig. 8. Fig. 8. Statistical distribution and pixel numbers of NDVI(N) at 21 elevation difference (ED) grades in the eight UAV control flying areas for the two land use types."–" represents the maximum and minimum of the data set; the upper and lower boundaries of the box represent the upper quartile (75%) and the lower quartile (25%), respectively; and the rectangle represents the median of the data set.

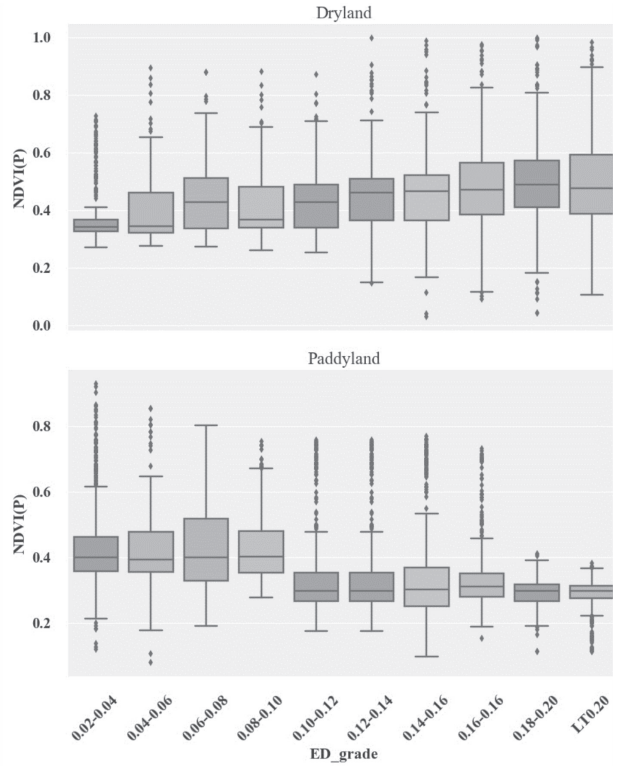

Fig. 9. Statistical distribution and pixel numbers of NDVI(P) at 21 elevation difference (ED) grades in the eight UAV control flying areas for the two land use types."–" means the max and min of the data set; the upper and lower of the box represent the upper 75% and the lower 25%; and the rectangle represents the median of the data set.

NDVI(P) value is in the range of 0.47–0.61. The ED grade of 0.12–0.14 m is the threshold in dry land, i.e., there is more P in the soil at ED grades higher than this threshold. In paddy land, the trend of the distribution of NDVI(P) values is markedly different than that in dry land, i.e., there are more pixels with high values located at low ED grades. The average NDVI(P) value in paddy land is in the range of 0.31–0.43. This means there is more soil P in paddy land with low ED grades, similar to the distribution law of NDVI(N). The threshold of NDVI(P) distribution variation in paddy land is 0.08–0.10 m; however, the magnitude of the variation is smaller than that of NDVI(N).

At the microtopographic scale, paddy land with low ED has high soil N and P concentrations, while land with higher EDs has less soil N and P concentrations (Figs 8 and 9). This result is consistent with the conclusions of previous studies that found that topography influences the concentrations and spatial distributions of both soil N [55] and soil P concentrations [56]. Different from previous studies, we used topographic data with higher resolution, and the methods we used to survey the status and concentrations of soil N and P at 21 ED grades were more efficient. At the same time, the influence of temporal accumulation should also be considered at this scale. Topography can directly influence runoff confluence, even in flat agricultural areas, and this changes the destination of resolved soil nutrients such as nitrate nitrogen, ammonium nitrogen, and Olsen-P [14]. Soil erosion also exists at the microtopographic scale, and sediments, together with adsorbed nutrients, are transported along the slopes of small EDs [14, 57]. The influence of temporal accumulation should also be considered at the microtopographic scale because slight changes transmitted from the external environment affect soil N and P concentrations, e.g., routine irrigation or moderate rainfall. Precipitation and soil erosion processes should be considered in relation to soil nutrient loss. In dry land, soil P was found to have a different spatial distribution across the ED grades to N. This was because dry land is irrigated by rainfall, and P has stronger adsorption capability than N; thus, it cannot be transported easily by water flow derived only from rainfall.

Remote sensing data derived from space (GF-2) and aerial (UAV) platforms were used synergistically with in-situ experimental data in this study. This generated some uncertainty in the results because of the different scales of these data and precision loss from data processing. Scale issues, which include upscaling and downscaling processes, are always intractable problems inherent in remote sensing science [58]. Remote sensing data of diverse land surface information can be collected on different scales. To present a simple and easily understandable result, we processed multiscale remote sensing data to a single scale, which may have resulted in some loss of information regarding the land surface. For example, in this research, the satellite remote sensing data were downscaled, whereas the UAV and in-situ experimental data were upscaled. However, the synergistic use of multisource remote sensing data provides a new method to explore the relations between microtopography and soil N and P. Undoubtedly, some elements of this study could be improved. At the microtopographic scale, to explain the effects of topography on soil N and P, researchers should focus on the remolding of runoff confluence, soil erosion, and sediment transport to topography.

This research can be a very good guide for other studies on small-scale soil N/P concentrations. The high-resolution topographic data from the UAV and the two new indices (NDVI(N) and NDVI(P)) used in this study have implications regarding soil nutrient management, prevention of nonpoint source pollution, and development of precision agriculture. Furthermore, this method will exhibit better performance when kept away from fertilization time because this can minimize the influence of fertilization on quantifying the relationship between microtopography and N and P. UAV has advantages in that it can be used to obtain targeted data with high spatiotemporal resolution both rapidly and economically [35]. When such data are used in combination with the two proposed indices, the N and P loss paths can be established and CSAs can be detected. Once CSAs have been determined, the paths of nonpoint source pollution can be detected and

pollution prevention will become much easier. Precision agriculture can also benefit from this method. The soil N and P concentrations in each pixel and at every ED grade can be fully comprehended based on the two new indices; thus, this new method can provide better understanding regarding the process of soil nutrient loss and the detection of CSAs.

Conclusions

This study explored the relationships between microtopography and soil N and P concentrations by incorporating UAV and GF-2 remote sensing data. The results revealed that more pixels have high NDVI(N) values distributed at low ED grades in paddy land, whereas the opposite is observed in dry land. This means there is more N in the soil at low ED grades in paddy land and high elevation difference grades in dry land. Compared with NDVI(N), there are more NDVI(P) pixels with high values at high elevation difference grades in dry land and more pixels with small values at low elevation difference grades in paddy land. The results indicate that microtopography can redistribute N and P spatially within the soil because it changes the direction of flow from irrigation and rainfall and of sediment flow from erosion. Furthermore, NDVI(N) and NDVI(P) were found to have a positive correlation (R^2 = 0.75), suggesting that N and P accumulate simultaneously in the soil of agricultural land. The findings of this study highlight the efficacy of a new method that could be used both for preventing nonpoint source pollution and for elucidating processes relevant to soil nutrient management and precision agriculture.

Acknowledgements

We acknowledge all of the editors and reviewers for their valuable advice. The authors would also like to thank the financial support from National Natural Science Foundation of China (Grant Nos. 41801334,U1812401, U1603241, 41875044), Natural Science Foundation of Beijing (8192021), the financial support from the China Postdoctoral Science Foundation (2017M620663), the Fundamental Research Funds for the Central Universities (2017NT11), the National Key Project for R&D (No. 2018YFC0407900).

References

1. AMUNDSON R., BERHE A.A., HOPMANS J.W., OLSON C., SZTEIN A.E., SPARKS D.L. Soil and human security in the 21st century. Science. **348** (6235), 1261071, **2015**.
2. DUNNE T., ZHANG W., AUBRY B.F. Effects of rainfall, vegetation, and microtopography on infiltration and runoff. Water Resources Research. **27** (9), 2271, **1991**.
3. LAURANCE S.G., LAURANCE W.F., ANDRADE A., FEARNSIDE P.M., HARMS K.E., VICENTINI A., LUIZÃO R.C. Influence of soils and topography on Amazonian tree diversity: a landscape-scale study. Journal of Vegetation Science. **21** (1), 96, **2010**.
4. DAMASCO G., VICENTINI A., CASTILHO C.V., PIMENTEL T.P., NASCIMENTO H.E. Disentangling the role of edaphic variability, flooding regime and topography of Amazonian white-sand vegetation. Journal of Vegetation Science. **24** (2), 384, **2013**.
5. ZHU Q., SCHMIDT J. P., BRYANT R. B. Maize (*Zeamays* L.) yield response to nitrogen as influenced by spatio-temporal variations of soil–water-topography dynamics. Soil and Tillage Research. **146**, 174-183, **2015**.
6. SHARPLEY A., KLEINMAN P. Effect of rainfall simulator and plot scale on overland flow and phosphorus transport. Journal of Environmental Quality. **32** (6), 2172, **2003**.
7. CETIN M., SEVIK H., CANTURK U., CAKIR C. Evaluation of the recreational potential of Kutahya Urban Forest. Fresenius Environmental Bulletin. **27** (5), 2629, **2018**.
8. CETIN M., ZEREN I., SEVIK H., CAKIR C., AKPINAR H. A study on the determination of the natural park's sustainable tourism potential. Environmental Monitoring and Assessment. **190** (3), 167, **2018**.
9. CETIN M., ADIGUZEL F., KAYA O., SAHAP A. Mapping of bioclimatic comfort for potential planning using GIS in Aydin. Environment, Development and Sustainability. **20** (1), 361, **2018**.
10. LOU H., YANG S., ZHAO C., ZHOU Q., BAI J., HAO F., WU L. Phosphorus risk in an intensive agricultural area in a mid-high latitude region of China. Catena. **127**, 46, **2015**.
11. LIU R., XU F., ZHANG P., YU W., MEN, C. Identifying non-point source critical source areas based on multi-factors at a basin scale with SWAT. Journal of Hydrology. **533**, 379, **2016**.
12. SHARPLEY A.N., KLEINMAN P.J., FLATEN D.N., BUDA A.R. Critical source area management of agricultural phosphorus: experiences, challenges and opportunities. Water Science and Technology. **64** (4), 945, **2011**.
13. HAHN C., PRASUHN V., STAMM C., MILLEDGE D. G., SCHULIN R. A comparison of three simple approaches to identify critical areas for runoff and dissolved reactive phosphorus losses. Hydrology and Earth System Sciences. **18** (8), 2975, **2014**.
14. KOVACS A., HONTI M., ZESSNER M., EDER A., CLEMENT A., BLÖSCHL G. Identification of phosphorus emission hotspots in agricultural catchments. Science of the Total Environment. **433**, 74, **2012**.
15. LEI T., WU J., LI X., GENG G., SHAO C., ZHOU H., WANG Q., LIU L. A new framework for evaluating the impacts of drought on net primary productivity of grassland. Science of the Total Environment. **536**, 161, **2015**.
16. SEVIK H., CETIN M. Effects of water stress on seed germination for select landscape plants. Polish Journal of Environmental Studies **24** (2), 6893, **2015**.
17. KAYA E., AGCA M., ADIGUZEL F., CETIN M. Spatial data analysis with R programming for environment. Human and Ecological Risk Assessment: An International Journal. **25** (6), 1521, **2019**.
18. BOZDOGAN SERT E., TURKMEN M., CETIN M. Heavy metal accumulation in rosemary leaves and stems

exposed to traffic-related pollution near Adana-İskenderun Highway (Hatay, Turkey), Environmental Monitoring and Assessment. **191**, 553, **2019**.
19. KAHILUOTO H., KUISMA M., KETOJA E., SALO T., HEIKKINEN J. Phosphorus in manure and sewage sludge more recyclable than in soluble inorganic fertilizer. Environmental science & technology. **49** (4), 2115, **2015**.
20. LOU H., YANG S., ZHAO C., WANG Z., SHI L., WU L., DONG G., CAI M., HAO F., SUN Y. Using a nitrogen-phosphorus ratio to identify phosphorus risk factors and their spatial heterogeneity in an intensive agricultural area. Catena. **149**, 426, **2017**.
21. NEARING M.A., JETTEN V., BAFFAUT C., CERDAN O., COUTURIER A., HERNANDEZ M., BISSONNAISE Y, NICHOLS M., NUNES J., RENSCHLER C., SOUCHÈRE V. Modeling response of soil erosion and runoff to changes in precipitation and cover. Catena. **61** (2-3), 131, **2005**.
22. SHARPLEY A., JARVIE H. P., BUDA A., MAY L., SPEARS B., KLEINMAN P. Phosphorus legacy: Overcoming the effects of past management practices to mitigate future water quality impairment. Journal of Environmental Quality. **42** (5), 1308, **2013**.
23. LOU H., YANG S., ZHAO C., SHI L., WU L., WANG Y., WANG Z. Detecting and analyzing soil phosphorus loss associated with critical source areas using a remote sensing approach. Science of The Total Environment. **573**, 397, **2016**.
24. SHRUTHI R.B., KERLE N., JETTEN V., ABDELLAH L., MACHMACH I. Quantifying temporal changes in gully erosion areas with object oriented analysis. Catena. **128**, 262, **2015**.
25. HENG B.C.P., SANDER G.C., ARMSTRONG A., QUINTON J.N., CHANDLER J.H., SCOTT C.F. Modeling the dynamics of soil erosion and size-selective sediment transport over nonuniform topography in flume-scale experiments. Water Resources Research. **47** (2), **2011**.
26. WU L., LONG T.Y., LIU X., GUO J.S. Impacts of climate and land-use changes on the migration of non-point source nitrogen and phosphorus during rainfall-runoff in the Jialing River Watershed, China. Journal of hydrology. **475**, 26, **2012**.
27. SONNEVELD M.P. W., SCHOORL J.M., VELDKAMP A. Mapping hydrological pathways of phosphorus transfer in apparently homogeneous landscapes using a high-resolution DEM. Geoderma. **133** (1), 32, **2006**.
28. JIANG F., WU X., XIANG W., FANG X., ZENG Y., OUYANG S., LEI P., DENG X., PENG C. Spatial variations in soil organic carbon, nitrogen and phosphorus concentrations related to stand characteristics in subtropical areas. Plant and Soil. 1-13, **2016**.
29. SHEN Z., CHEN L., HONG Q., QIU J., XIE H., LIU R. Assessment of nitrogen and phosphorus loads and causal factors from different land use and soil types in the Three Gorges Reservoir Area. Science of the total environment. **454**, 383, **2013**.
30. LI X., CHANG S. X., LIU J., ZHENG Z., WANG X. Topography-soil relationships in a hilly evergreen broadleaf forest in subtropical China. Journal of Soils and Sediments. 1-15, **2016**.
31. RODRIGUEZ E., MORRIS C.S., BELZ J.E. A global assessment of the SRTM performance. Photogrammetric Engineering & Remote Sensing. **72** (3), 249, **2006**.
32. RANGO A., LALIBERTE A., HERRICK J.E., WINTERS C., HAVSTAD K., STEELE C., BROWNING D. Unmanned aerial vehicle-based remote sensing for rangeland assessment, monitoring, and management. Journal of Applied Remote Sensing. **3** (1), 033542, **2009**.
33. BRYSON M., REID A., RAMOS F., SUKKARIEH S. Airborne vision-based mapping and classification of large farmland environments. Journal of Field Robotics. **27** (5), 632, **2010**.
34. HUSSON E., HAGNER O., ECKE F. Unmanned aircraft systems help to map aquatic vegetation. Applied vegetation science. **17** (3), 567, **2014**.
35. CATUREGLI L., CORNIGLIA M., GAETANI M., GROSSI N., MAGNI S., MIGLIAZZI M., ANGELINI L., MAZZONCINI M., SILVESTRI N., FONTANELLI M., RAFFAELLI M., PERUZZI A., VOLTERRANI M. Unmanned aerial vehicle to estimate nitrogen status of turfgrasses. PloS one. **11** (6), e0158268, **2016**.
36. KARA D., OZSAVASCI C., ALKAN. Investigation of suitable digestion methods for the determination of total phosphorus in soils. Talanta. **81** (1), 75, **1997**.
37. SARAVIA D., FARFÁN-VIGNOLO E. R., GUTIÉRREZ R., MENDIBURU F., SCHAFLEITNER R., BONIERBALE M., KHAN M.A. Yield and Physiological Response of Potatoes Indicate Different Strategies to Cope with Drought Stress and Nitrogen Fertilization. American Journal of Potato Research. 1-8, **2016**.
38. HITZ K., CLARK A.J., VAN SANFORD D.A. Identifying nitrogen-use efficient soft red winter wheat lines in high and low nitrogen environments. Field Crops Research. **200**, 1, **2017**.
39. PANDEY P.C., MANDAL V.P., KATIYAR S., KUMAR P., TOMAR V., PATAIRIYA S., RAVISANKAR N., GANGWAR B. Geospatial Approach to Assess the Impact of Nutrients on Rice Equivalent Yield Using MODIS Sensors'-Based MOD13Q1-NDVI Data. IEEE Sensors Journal. **15** (11), 6108, **2015**.
40. LIN C., MA R., ZHU Q., LI J. Using hyper-spectral indices to detect soil phosphorus concentration for various land use patterns. Environmental monitoring and assessment. **187** (1), 1, **2015**.
41. WANG J., SHI T., LIU H., WU G. Successive projections algorithm-based three-band vegetation index for foliar phosphorus estimation. Ecological Indicators. **67**, 12, **2016**.
42. ARNALL D.B., ABIT M.J.M., TAYLOR R.K., RAUN W.R. Development of an NDVI-Based Nitrogen Rate Calculator for Cotton. Crop Science. **56** (6), 3263, **2016**.
43. LIU C., YANG S., WEN Z., WANG X., WANG Y., LI Q., SHENG H. Development of ecohydrological assessment tool and its application. Science in China Series E: Technological Sciences. **52** (7), 1947, **2009**.
44. NEITSCH S.L., ARNOLD J.G., KINIRY J.R., WILLIAMS J.R. Soil and water assessment tool theoretical documentation version 2009. Texas Water Resources Institute. **2011**.
45. HEINEN M. Simplified denitrification models: overview and properties. Geoderma. **133** (3-4), 444, **2006**.
46. JONES C.A., COLE C.V., SHARPLEY A.N., WILLIAMS J.R. A simplified soil and plant phosphorus model: I. Documentation 1. Soil Science Society of America Journal. **48** (4), 800, **1984**.
47. ZHU W.Q., PAN Y.Z., ZHANG J.S. Estimation of net primary productivity of Chinese terrestrial vegetation based on remote sensing. Journal of Plant Ecology. **31** (3), 413, **2007**.
48. ZHU Z., ARP P.A., MENG F., BOURQUE C.P.A., FOSTER N.W. A forest nutrient cycling and biomass

model (ForNBM) based on year-round, monthly weather conditions, part I: assumption, structure and processing. Ecological Modelling. **169** (2-3), 347, **2003**.
49. ARAI K., SAKASHITA M., SHIGETOMI O., MIURA Y. Relation between Rice Crop Quality (Protein Content) and Fertilizer Amount as Well as Rice Stump Density Derived from Helicopter Data. Relation. **4** (7), **2015**.
50. ZHENG H., CHENG T., YAO X., DENG X., TIAN Y., CAO W., ZHU Y. Detection of rice phenology through time series analysis of ground-based spectral index data. Field Crops Research. **198**, 131, **2016**.
51. KIM J., GRUNWALD S. Assessment of Carbon Stocks in the Topsoil Using Random Forest and Remote Sensing Images. Journal of Environmental Quality. **45** (6), 1910, **2016**.
52. MOUAZEN A.M., KUANG B. On-line visible and near infrared spectroscopy for in-field phosphorous management. Soil and Tillage Research. **155**, 471, **2016**.
53. GOODCHILD M.F., GLENNON J.A. Crowdsourcing geographic information for disaster response: a research frontier. International Journal of Digital Earth. **3** (3), 231, **2010**.
54. STEWART K.J., GROGAN P., COXSON D.S., SICILIANO S.D. Topography as a key factor driving atmospheric nitrogen exchanges in arctic terrestrial ecosystems. Soil Biology and Biochemistry. **70**, 96, **2014**.
55. HARMS T.K., EDMONDS J.W., GENET H., CREED I.F., ALDRED D., BALSER A., JONES J.B. Catchment influence on nitrate and dissolved organic matter in Alaskan streams across a latitudinal gradient. Journal of Geophysical Research: Biogeosciences. **121** (2), 350, **2016**.
56. ARAÚJO M.S., SCHAEFER C.E., SAMPAIO E.V. Soil phosphorus fractions from toposequences of semi-arid Latosols and Luvisols in northeastern Brazil. Geoderma. **119** (3), 309, **2004**.
57. BUTLER D.M., FRANKLIN D.H., RANELLS N.N., POORE M.H., GREEN J.T. Ground cover impacts on sediment and phosphorus export from manured riparian pasture. Journal of environmental quality. **35** (6), 2178, **2006**.
58. GONZÁLEZ-ROGLICH M., SWENSON J.J. Tree cover and carbon mapping of Argentine savannas: Scaling from field to region. Remote Sensing of Environment. **172**, 139, **2016**.